

Supplementary Information:

Deviations from Vegard's Law and Evolution of the Electrocatalytic Activity and Stability of Pt-Based Nanoalloys Inside Fuel Cells by *in Operando* X-ray Spectroscopy and Total Scattering

Valeri Petkov,^{†,*} Yazan Maswadeh,[†] Jorge Vargas Tellez,[†] Shiyao Shan,[§] Haval Kareem,[§] Zhipeng Wu,[§] Jin Luo,[§] Chuan-Jian Zhong,[§] Sarvjit Shastri[‡] and Peter Kenesei[‡]

[†]Department of Physics and Science of Advanced Materials Program, Central Michigan University, Mt. Pleasant, Michigan 48859, United States

[§]Department of Chemistry, State University of New York at Binghamton, Binghamton, New York 13902, USA

[‡]X-ray Science Division, Advanced Photon Source, Argonne National Laboratory, Argonne, Illinois 60439, United States

i) Synthesis of binary and ternary Pt-TM nanoalloy catalysts (TM=Ni, Co and Cu).

Binary and ternary Pt-TM nanoalloys, where TM=Ni, Co and Cu, were synthesized by a one-pot route reported in Refs. [S1, S2]. It involved mixing relevant metal precursors, in particular Pt^{II}(acetoacetate)₂, Ni^{II}(acetoacetate)₂, Co^{III}(acetoacetate)₃, CuCl₂ and/or Cu^{III}(acetoacetate) in pre-desired molar ratios into octyl ether solvent. Oleylamine and oleic acid were added into the solutions and used as capping agents. 1,2-hexadecanediol was also added and used as a reducing agent. The solutions were purged with N₂ and heated to 105 °C. At this temperature the purging with N₂ was discontinued, the mixtures heated to 280 °C and refluxed for 40 min. The solutions were then cooled back to room temperature and the resulting Pt-TM alloy nanoparticles (NPs) were precipitated out by adding ethanol followed by centrifugation. The NPs were dried under N₂ atmosphere and re-dispersed in a solution of fine carbon powder (XC-72) in hexane. Furthermore, the NPs were post-synthesis treated at 260 °C under N₂ atmosphere for 30 min followed by calcination at 400 °C under 15 vol% H₂ atmosphere for 2 h. The treatment is necessary to remove the organic capping agents from the NP's surface and improve the degree of alloying of Pt and TM species in the NPs. Hereafter, the post-synthesis treated NPs are referred to as fresh NPs.

ii) *Determining the average chemical composition, size and shape of Pt-TM nanoalloy catalysts.*

The overall chemical composition of the fresh and electrochemically cycled (~1500 cycles/300 min) Pt-TM NPs was determined by inductively coupled plasma atomic emission spectroscopy (ICP-AES). Measurements were done on a Perkin Elmer 2000 DV ICP-AES instrument. Calibration was done against standards dissolved in the same acid matrix as the unknowns. Several batches of the unknowns were analysed thus ensuring < 2 % error in the overall chemical composition. Experimental data showed that the average chemical composition of the fresh binary and ternary alloy Pt-Ni/Co NPs is Pt₆₈Co₃₂, Pt₅₈Ni₁₇Co₂₅, Pt₃₇Ni₃₉Co₂₄ and Pt₁₂Ni₅₃Co₃₅. Upon undergoing 1500 potential cycles inside a proton exchange membrane fuel cell (PEMFC), the NPs appeared with a chemical composition of Pt₈₁Co₁₉, Pt₇₂Ni₁₆Co₁₂, Pt₅₈Ni₁₆Co₂₆ and Pt₄₅Ni₃₆Co₁₉, respectively. The average chemical composition of the fresh Pt-Ni-Cu alloy NPs turned out to be Pt₂₁Ni₄₀Cu₃₉ and Pt₅₁Co₁₈Cu₃₁. That of cycled Pt-Ni-Cu alloy NPs appeared Pt₄₄Ni₃₂Cu₂₄ and Pt₆₆Co₁₅Cu₁₉, respectively. The ICP-AES data were confirmed by independent energy dispersive x-ray spectroscopy (EDS) experiments described below.

The size and shape of the fresh Pt-TM alloy NPs were determined by Transmission Electron Microscopy (TEM) on a JEM-2200FS instrument operated at 200 kV. Exemplary TEM and high-resolution (HR)-TEM images for Pt-Ni/Co/Cu alloy NPs are shown in Figure S1. As can be seen in the Figure, the NPs are approximately 8.7 (±1.5) nm in size and largely spherical in shape. Furthermore, lattice fringes seen in the HR-TEM images indicate that the NPs possess a good degree of crystallinity.

iii) *Studies on the performance of Pt-TM nanoalloys as catalysts for ORR under actual operating conditions*

A fully functional PEMFC optimized for simultaneous EDS and high-energy x-ray diffraction (HE-XRD) experiments was used to study the concurrent changes in the chemical composition, atomic structure and catalytic activity of Pt-TM alloy NPs under realistic operating conditions. The PEMFC is shown in Figure S2. Membrane electrode assemblies (MEAs) for the PEMFC were prepared using fresh pure Pt (E-tek) and Pt-TM alloy NPs as ORR (oxygen reduction reaction) catalysts. Standard Pt NPs (E-tek) were used as a HOR (hydrogen oxidation reaction) catalyst. For reference, the ORR and HOR take place at the PEMFC cathode and anode, respectively. In particular, the respective NPs were dissolved in a Nafion-containing solution and

then brush coated on (2.5 cm x 2.5 cm) pieces of a wet-proof carbon paper (Spectracarb). The ORR and HOR catalyst coated pieces of carbon paper were fused to the opposite sides of a Nafion membrane (DuPont) by hot pressing at 120 °C. The resulting sandwich-type {Carbon Paper-HOR Catalyst-Nafion Membrane-ORR Catalyst-Carbon Paper} MEA assemblies were transferred to the custom-made PEMFC and cycled between 0.6 V and 1.0 V for 5 to 6 hours, following a protocol suggested by DOE.^{S3, S4} In total, the catalyst particles underwent about 1600 potential cycles as deposited on the cathode side of MEAs. During the cycling, high purity hydrogen (3.5% H₂ balanced by N₂) and nitrogen gas was fed to the PEMFC anode and cathode compartments, respectively, at a rate of 50 mL/min. Before reaching the PEMFC, the gases were forced through water bubblers to achieve 100 % humidity and heated up to about 80 °C. In addition, the plastic gas delivery tubes were thermally protected. A heater wrapped around the PEMFC (clearly seen in Figure S2) was used to keep its operating temperature as close to 80 °C (± 5 °C) as possible. Hence, and per our observations, the PEMFC was never let dry during the potential cycling. The current output of the PEMFC was non-stop recorded during the potential cycling. Experimental polarization curves (~1600 in number) representing the current output of the PEMFC resulted from the repetitive application of external voltages are summarized in Figure 1. Selected polarization curves are shown in Figure S3. In line with the practices of *ex situ* catalytic studies,^{S5-S10} the current output of the PEMFC at a fixed voltage value, in particular at 0.9 V on the polarization curves, was used to assess the electrocatalytic activity of the respective nanoalloys. The rationale is that this output is sensitive to the formation and reduction of oxygenated surface species, such as Pt(O) and Pt(OH), which are an important factor in determining the kinetics of ORR over the surface Pt-TM nanoalloys.

In particular, without loss of generality, the catalyzed electrochemical reduction of oxygen to water (ORR) taking place at the cathode of PEMFCs can be described as $O_2 + 4H^+ + 4e^- \rightarrow H_2O$. A widely accepted view is that atomic-level changes of Pt-TM nanoalloy catalysts that would prevent ORR intermediates, such as Pt(O) and Pt(OH), from blocking O₂ adsorption sites would have a positive impact on the ORR kinetics, i.e. improve the activity of nanoalloys as ORR catalysts, and vice versa. To be more precise, the ORR current, i_{ORR} , generated in the PEMFC cathode catalyst layer at a particular potential, U , temperature, T , and concentration of the reactants is considered to dependent strongly on the coverage, θ , of the catalyst surface with reactive intermediates as follows:

$$i_{ORR} \sim i_o(1-\theta) \exp(-\gamma\Delta G/RT)\exp(-\beta FU/RT), \quad (S1)$$

where i_o is the so-called exchange current density, ΔG is the Gibbs energy of adsorption and β , γ , F and R are constants.^{S7} Notably, θ values are assessed through studying Pt-TM nanoalloys under humidified N₂ atmosphere. That is because studies have indicated that i) the exposure of Pt-based catalysts to humidified O₂ vs. humidified N₂ gas would not make much difference on the degree of oxidation of their top surface during (0.6 V-1.0 V) potential cycling and ii) typically, the removal of the oxygenated species is the step limiting the kinetics of both reactions.^{S11-S15} Logically, changes in the “redox” current at 0.9 V on the polarization curves measured under humidified N₂ atmosphere were considered as a measure of changes in θ , i.e., relative number of surface Pt atoms capable of reducing O₂, and, hence, in the electrocatalytic activity of the respective nanoalloys. Here is to be noted that the i_{ORR} current at 0.9 V is indeed very weak (see Figure S3) and so possible IR (resistive-type) losses are minimized. Nevertheless, we measured the PEMFC resistance under 100 % H₂ and 3.5 % H₂ atmosphere in the anode compartment and found that the former was smaller than the latter by 0.5 Ω . This would have resulted in an IR drop of no more than 50 mV. We also evaluated the IR drop possibly resulting from deteriorated thermal protection of the gas delivery tubes and found that it would be in the order of 30-50 mV. Such IR drops would have little impact on the results reported here because the potential range for the PEMFC cycling would not change much, which is important for the *in operando* measurements. Regardless, we did not attempt to extract absolute values for the electrocatalytic activity of Pt-TM nanoalloys from the *in operando* polarization curves. That is because studies have shown that, due to intrinsic differences (e.g. in pH, temperature, humidity, catalyst environment/support, PEMFC configuration and MEAs preparation) between laboratory and fuel cell measurements for ORR catalyst testing, full quantitative agreement between measures for electrocatalytic activity, including its changes, derived from data obtained under laboratory and operating conditions cannot be expected. It is important though that trends between different catalysts and with respect to their aging behavior are correctly represented.^{S15} Hence, changes in the “redox” current at 0.9 V on the polarization curves with the potential cycling were represented in terms of percentage differences from the initial value of the current and considered merely as a quantity describing relative changes in the apparent (as measured) ORR activity of cycled nanoalloys as deposited on MEAs. Relative changes in ORR activity derived as described above were cross-checked against similarly normalized data for changes in

ORR activity obtained on a standard 3-electrode cell. Results from the comparison are shown in Figure S5. As can be seen in the Figure, overall, trends of data for relative changes in ORR activity of Pt-TM nanoalloys obtained by laboratory and *in operando* experiments agree, testifying to the reliability of the results reported here. In addition, changes in ORR activity (decay) derived as described above were compared with relative changes in the area of respective polarization curves (collapsing) with the potential cycling, which are related to relative changes in the oxidation/reduction charge during the cycling. Results are shown in Figure S4. As can be seen in the Figure, trends in the both sets of data provide a consistent picture of the evolution of the apparent ORR activity of Pt-TM nanoalloys during the PEMFC operation.

iv) In-operando energy-dispersive x-ray spectroscopy (EDS) experiments

Changes in the elemental composition of Pt-TM alloy NPs under the corrosive conditions at the cathode of the operating PEMFC were determined by EDS spectroscopy. EDS spectra were taken simultaneously with the HE-XRD patterns, *i.e.*, in intervals of 1 min, using a Si Vortex detector coupled to a multi-channel analyzer. The spectra were processed and elemental composition determined using standard procedures.^{S17} Exemplary EDS spectra for Pt-Ni/Co alloy NPs are shown in Figure S7. Changes in the average chemical composition of Pt-TM alloy NPs (TM=Ni, Co) with the potential cycling are summarized in Figure 6. Changes in the chemical composition and mass distribution (loading) of the catalyst particles over the PEMFC cathode occurring during the potential cycling were also investigated by scanning a 4.5 mm by 4.5 mm area of the respective MEAs with a narrow collimated x-ray beam (40 μm by 20 μm). Exemplary maps showing the elemental composition and loading of fresh and cycled monometallic (pure Pt), bimetallic ($\text{Pt}_{81}\text{Co}_{19}$) and ternary ($\text{Pt}_{12}\text{Ni}_{53}\text{Co}_{35}$) catalyst particles over the scanned area shown in Figures 2, 3 and S8, respectively.

v) In-operando total x-ray scattering experiments

Atomic-level changes of pure Pt and Pt-TM alloy NPs (TM=Ni, Co, Cu) functioning as ORR catalysts at the cathode of a PEMFC were studied by x-ray total scattering experiments involving high-energy x-ray diffraction (HE-XRD) coupled to atomic pair distribution function (PDF) analysis. Experiments were done at the 1-ID-C beamline of the Advanced Photon Source at the Argonne National Laboratory. X-rays with energy of 84.917 keV ($\lambda=0.1458 \text{ \AA}$) and a large area

detector (see Figure S2) were used. HE-XRD patterns were collected in intervals of 1 min throughout the PEMFC operation (potential cycling). HE-XRD data for both the “empty” PEMFC (no MEA) and the PEMFC with a MEA containing the anode catalyst alone were taken separately. The data were used to correct the HE-XRD patterns for the catalyst particles collected during the PEMFC operation. *In operando* HE-XRD patterns for pure Pt and Pt-TM nanoalloy catalysts are summarized in Figure 1. As can be seen in the Figure, the HE-XRD patterns exhibit a few strong, Bragg-like peaks at low diffraction angles and almost no sharp features at high diffraction angles. This rendered the well-established, sharp Bragg peaks-based procedures for characterizing the 3D atomic structure of bulk metals and alloys difficult to apply to the ORR catalysts studied here. Therefore, *in operando* HE-XRD patterns were analysed in terms of atomic PDFs which have proven very useful in structure studies of metallic NPs.^{S18,S19} Derivation of atomic PDFs from HE-XRD patterns is described in Section vi) below. Note that for a given amount of atomic species in a spherical NP, the surface area that can be associated with the species, usually referred to as a geometric surface area (GSA), is inversely proportional to the diameter, *i.e.* size of the NP. Studies have shown that, in general, the GSA and the so-called electrochemical active surface area (ECSA) of metallic NPs used as ORR catalysts are related to each other. Hence, changes in the former can be used as a relative measure of changes in the latter.^{S20,S21} The average size of fresh and cycled pure Pt and Pt-TM alloy NPs was determined from the full width at half maximum (FWHM) of the strongest Bragg-like peak in the respective *in operando* HE-XRD patterns using the Scherrer formalism.^{S22} As it may be expected, results showed that the cycled NPs grow in size, that is, their GSA decreases during the PEMFC operation.^{S3,S23} Changes in the GSA of cycled NPs during the PEMFC operation are summarized in Figure 6.

vi) *Derivation and interpretation of atomic PDFs for Pt-TM nanoalloy catalysts*

Experimental *in operando* HE-XRD patterns for pure Pt and Pt-TM alloy NPs were corrected for experimental artifacts, in particular for the strong background-type scattering originating from the PEMFC hardware, and then used to derive the so-called total structure factors defined as:

$$S(q) = 1 + \left[I^{coh.}(q) - \sum c_i |f_i(q)|^2 \right] / \left| \sum c_i f_i(q) \right|^2, \quad (S2)$$

where $I^{coh.}(q)$ are the coherently scattered x-ray intensities, c_i and $f_i(q)$ are the concentration and x-ray scattering factor, respectively, for atomic species of type i , where $i = \text{Pt, Ni, Co and/or Cu}$.

The structure factors were Fourier transformed into the so-called total atomic PDFs, $G(r)$, as follows:

$$G(r) = \frac{2}{\pi} \int_{q=0}^{q_{max}} q[S(q) - 1] \sin(qr) dq, \quad (S3)$$

where q is the magnitude of the wave vector ($q=4\pi\sin\theta/\lambda$), 2θ is the angle between the incoming and outgoing x-rays, λ is the wavelength of x-rays used (0.1458 Å), r is the radial (real space) distance and q_{max} extends to 25 Å⁻¹. Experimental *in operando* atomic PDFs for pure Pt and Pt-TM alloy NPs are shown in Figure S6. Note that the Fourier transformation is a unitary operation and so does not alter in any way the atomic-structure relevant information contained in HE-XRD patterns.^{S18,S24}

As defined, the atomic PDF $G(r) = 4\pi r[\rho(r) - \rho_o]$, where $\rho(r)$ and ρ_o are the local and average atomic number density, respectively. Hence, $G(r)$'s peak at real space distances separating pairs of metal atoms, immediate and all farther neighbors, within the studied NPs. The area under the peaks is proportional to the number of atomic pairs at those distances. In particular, the first PDF peak reflects metal-to-metal atom bonding distances and coordination numbers. Furthermore, since surface atoms at the opposite sides of NPs are separated the most, PDF peaks at higher- r distances largely reflect pairs of atoms close to the NP surface. Therefore, experimental atomic PDFs are sensitive to the atomic-level structure throughout metallic NPs (typically < 15 nm) explored for catalytic applications, including the NP surface. This fact may not come as a surprise since i) atoms at the surface of such NPs occupy a substantial fraction of their overall volume (~ 30 % in the case of the NPs studied here) and ii) XRD is known to be sensitive to the volume fraction of the constituents of a metallic material down to a few %.

vii) X-ray photoelectron spectroscopy (XPS) studies on fresh Pt-TM alloy NPs

The electronic properties of near-surface Pt atoms in fresh Pt and Pt-TM alloy NPs were investigated by XPS. Measurements were done on a Kratos AXIS Ultra DLD spectrometer equipped with a monochromatic Al source. The spectrometer was calibrated using the C 1s peak at 284.8 eV, Cu 2p_{3/2} peak at 932.7 eV and Au 4f_{7/2} peak at 83.96 eV as internal standards. The pass energy was fixed at 20 eV for the detailed scans. Exemplary XPS Pt 4f spectra are shown in Figure S13. Data in the Figure indicate that, in addition to finite size effects, the electronic structure of Pt atoms changes with the type of TM atoms, and the change is different for the different NPs.

xi) 3D structure modeling

Structure models shown in Figures S10-S12 were built by MD simulations. The simulations were carried out with the help of computer program LAMMPS²⁴ under canonical NVT ensemble in the absence of periodic boundary conditions. Velocity Verlet algorithm with a time step of 2 fs was used. Initial model atomic configurations were equilibrated for 200 ps at 400 °C, which is just about the temperature at which Pt-TM alloy NPs were post-synthesis treated. The models were then cooled down to room temperature (300 K) in steps of 50 °C and again equilibrated for 100 ps.

Reverse Monte Carlo (RMC) simulations were used to refine further the MD generated models. In the spirit of RMC simulations, positions of atoms in the MD models were adjusted as to minimize the difference between the model computed and respective experimental atomic PDFs. During the simulations Pt and TM atoms were constrained both to maintain as maximal (i.e. as close to 12) as possible coordination numbers and, at the same time, not to come closer than pre-selected distances of closest approach (\sim the sum of their radii R_{ij}). The distances were determined from the positions of the first peak in the experimental atomic PDFs. During the simulations, model's energy was described by pair-wise potentials taken from literature sources and maintained as close as possible to its value achieved by MD. Nevertheless, when necessary, models underwent a sequence of MD and RMC runs. The success of the simulations was evaluated using a goodness-of fit indicator, R_w , described below. Simulations were done with the help of a new version of the program RMC++.²⁵ More details of modelling the 3D structure of metallic NPs by joint MD and RMC computations can be found in ref. [S19].

x) Evaluating the quality of model nanostructures for pure Pt and Pt-TM alloy NPs

The overall quality of tested model nanostructures was also evaluated by computing model's quality factors, R_w , defined as:^{S18,S24}

$$R_w = \left\{ \frac{\sum w_i (G_i^{\text{exp.}} - G_i^{\text{calc.}})^2}{\sum w_i (G_i^{\text{exp.}})^2} \right\}^{1/2} \quad (\text{S4})$$

where $G^{exp.}$ and $G^{calc.}$ are the experimental and model computed atomic PDFs, respectively, and w_i are weighting factors reflecting the experimental uncertainty of the individual $G^{exp.}$ data points. Here $w_i(G_i^{exp})$ were considered to be uniform which, as predicted by theory^{S21} and largely corroborated by experiment,^{S26-S28} is a reasonable approximation. Note that typical values of R_w for good quality structure models are in the order of 15-25 %.

SI References:

- S1. J. Yin, S. Shan, M. S. Ng, L. Yang, D. Mott, W. Fang, N. Kang, J. Luo and C. J. Zhong, *Langmuir*, 2013, **29**, 9249-9258.
- S2. Z. Yin, W. Zhou, Y. Gao, D. Ma, C. J. Kiely and X. Bao, *Chem-Eur J.* 2012, **18**, 4887- 4893.
- S3. R. Borup, J. Meyers, B. Pivovar, Y. S. Kim, R. Mukundan, N. Garland, D. Myers, M. Wilson, F. Garzon, D. Wood, P. Zelenay, K. More, K. Stroh, T. Zawodzinski, J. Boncella, J. E. McGrath, M. Inaba, K. Miyatake, M. Hori, K. Ota, Z. Ogumi, S. Miyata, A. Nishikata, Z. Siroma, Y. Uchimoto, K. Yasuda, K. I. Kimijima and N. Iwashita, *Chem. Rev.* 2007, **107**, 3904-3951.
- S4. F. Chang, S. Shan, V. Petkov, Z. Skeete, A. Lu, J. Ravid, J. Wu, J. Luo, G. Yu, Y. Ren and C. J. Zhong, *Electrochemistry* 2016, **84**, 511-515.
- S6. H. Schmies, A. Bergmann, J. Drnec, G. Wang, D. Teschner, S. Kühl, D. J. S. Sandbeck, S. Cherevko, M. Gocyla, M. Shviro, M. Heggen, V. Ramani, R. E. Dunin-Borkowski, K. J. J. Mayrhofer and P. Strasser, *Adv. Ener. Mater.* 2017, **4**, 1701663.
- S7. M. K. Debe, *Nature*, 2012, **486**, 43-51.
- S8. S. L. Koh, L. Jennifer, M. F. Toney and P. Strasser, *J. Phys. Chem. C* 2007, **111**, 3744-3752.
- S9. D. D. Papadias, R. K. Ahluwalia, N. Kariuki, D. Myers, K. L. More, D. A. Cullen, B. T. Sneed, K. C. Neyerlin, R. Mukundan and R. L. Borup, *J. Electrochem. Soc.* 2018, **165**, F3166-F3177.
- S10. C. A. Rice, P. Urchaga, A. O. Pistono, B. W. McFerrin, B. T. McComb and J. Hu, *J. Electrochem. Soc.* 2015, **162**, F1175-F1180.
- S11. R. Jinnouchi, K. Kodama, Y. Hatanaka and Y. Morimoto, *Phys. Chem. Chem. Phys.*, 2011, **13**, 21070–21083.
- S12. Y. Huang, J. Zhang, A. Kongkanand, F. T. Wagner, J. S. M. Li and J. Jornea, *Journal of The Electrochemical Society*, 2014, **161**, F10-F15.
- S13. S. Takahisa and Y. Morimoto, *Electrochemistry* 2016, **84**, 511-515.
- S14. M. Uchimura and S. Kocha, *Transactions*, 2007, **11**, 1215-1226.
- S15. V. Saveleva, V. Papaefthimiou, M. K. Daletou, V. H. Doh, C. Ulhaq-Bouillet, M. Diebold, S. Zafeiratos and L. R. Savinova, *J. Phys. Chem. C* 2016, **120**, 15930–15940.
- S16. S. Martens, L. Asen, G. Ercolano, Ch. Zalitis, A. Hawkins, A. M. Bonastre, L. Seidl, A. C. Knoll, J. Sharman, P. Strasser, D. Jones and O. Schneider, *J. Power Sources* 2018, **392**, 274-284.
- S17. D. E. Newbury, *Wiley*, 2002.
- S18. V. Petkov, *Mater. Today*, 2008, **11**, 28-38.
- S19. V. Petkov, B. Prasai, Y. Ren, S. Shan, J. Luo, P. Joseph and C. J. Zhong, *Nanoscale* 2014, **6**, 10048-10061.
- S20. E. F. Holby, W. Sheng, Y. Shao-Horn and D. Morgan, *Environ. Sci.* 2009, **2**, 865-871.

- S21. J. A. Gilbert, N. N. Kariuki, R. Subbaraman, A. J. Kropf, M. C. Smith, E. F. Holby, D. Morgan and D. J. Myers, *J. Am. Chem. Soc.* 2012, **134**, 14823-14833.
- S22. P. K. Klug and L. E. Alexander, *Wiley*, 1974.
- S23. H. A. Gasteiger, S. S. Kosta, B. Sompalli and F. T. Wagner *Appl. Catal. B: Environmental*, 2005, **56**, 9-35.
- S24. B. h. Toby and T. Egami, *Acta Cryst. A*, 1992, **48**, 336-346.
- S24. S. Plimpton, *J. Comp. Phys.* 995, **117**, 1-19. <http://lammmps.sandia.gov>
- S25. O. Gereben and V. Petkov, *J. Phys. Condens. Matter*, 2013, **25**, 454211.
- S26. L. B. Skinner, C. Huang, D. Schlesinger, L. G. M. Petterson, A. Nillson, C. J. Benmore, *J. Chem. Phys.*, 2013, **138**, 074506.
- S27. Y. Maswadeh, Y., Shan, S., Prasai, B., Zhao, Y., Xie, Z.-H., Wu, Z., Luo, J., Ren, Y., Zhong, C. J. and Petkov, *J. Mat. Chem. A* 2017, **5**, 7355-7365.
- S28. V. Petkov, B. Prasai, S. Shan, Y. Ren, J. Wu, H. Cronk, J. Luo **and** C. J. Zhong, *Nanoscale*, 2016, **20**, 10749-10767.

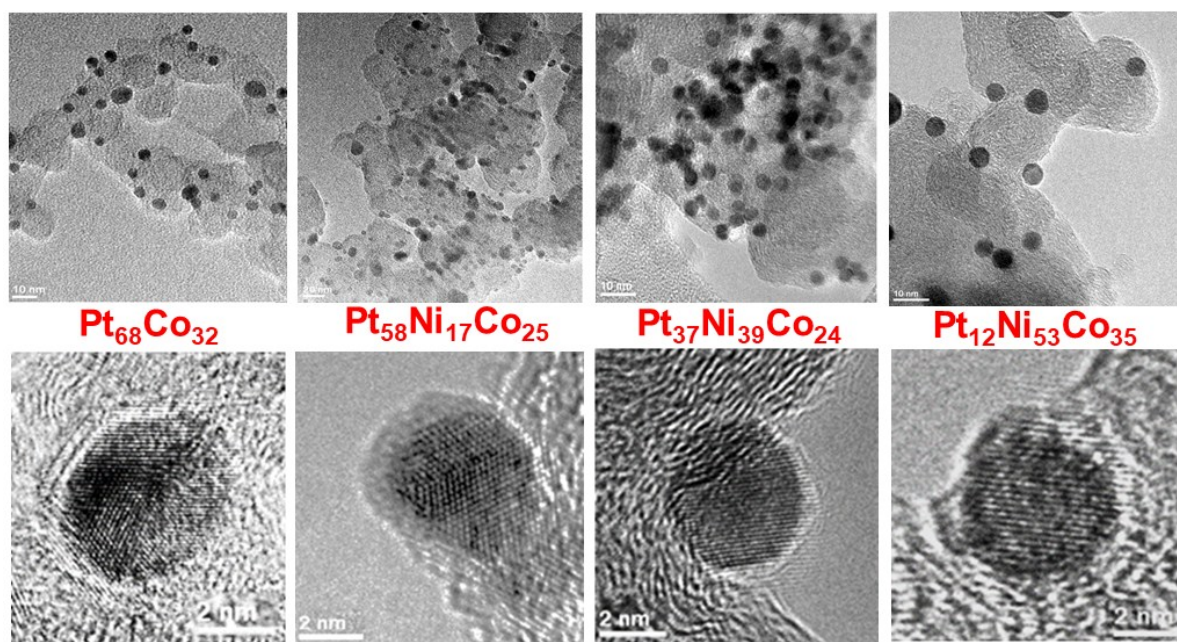
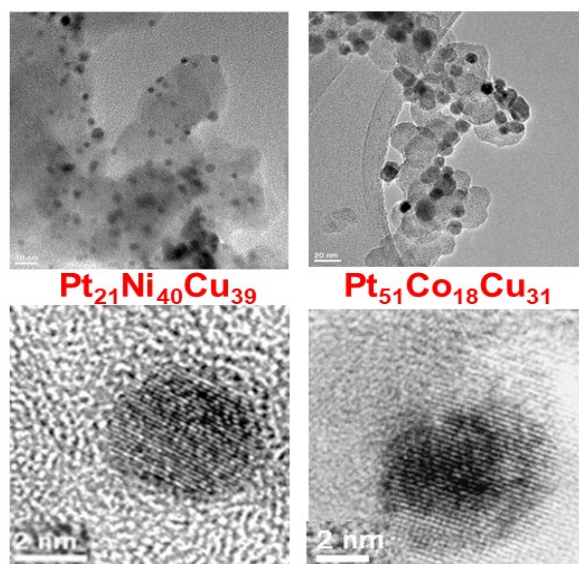


Figure S1. Representative TEM (first and third row) and HR-TEM (second and fourth row) images for fresh Pt-TM alloy NPs (TM=Ni, Co, Cu). The NPs appear with an average size of 8.7 (± 1.5) nm and rounded shape. Also, as the lattice fringes in the respective HR-TEM images indicate, the NPs are fairly crystalline. Note that the “ \pm ” deviation from the average NP size is the half width at full maximum of a gaussian-like distribution of sizes extracted from populations of several hundred NPs sampled by different TEM images. Size bars are highlighted for better visibility.



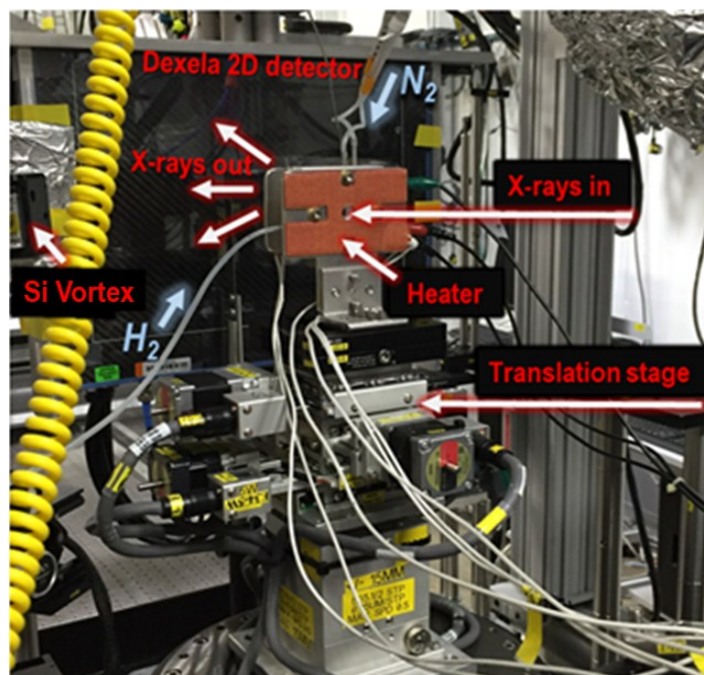


Figure S2. Custom-built PEMFC for *in operando* HE-XRD and EDS studies on ORR nanocatalysts as set up on a translation stage and used at the beam line 1-ID-C at the Advanced Photon Source, Argonne. The PEMFC cathode side looks into a 2D detector used to collect x-rays scattered from the PEMFC cathode (ORR) catalyst. A Si Vortex detector is used to collect EDS spectra from the catalyst. Gas lines supplying the PEMFC anode and cathode with H₂ and humidified N₂ gas, respectively, are clearly visible. A heater wrapped around the cell (in brown) helps maintain the PEMFC operating temperature at 80 °C.

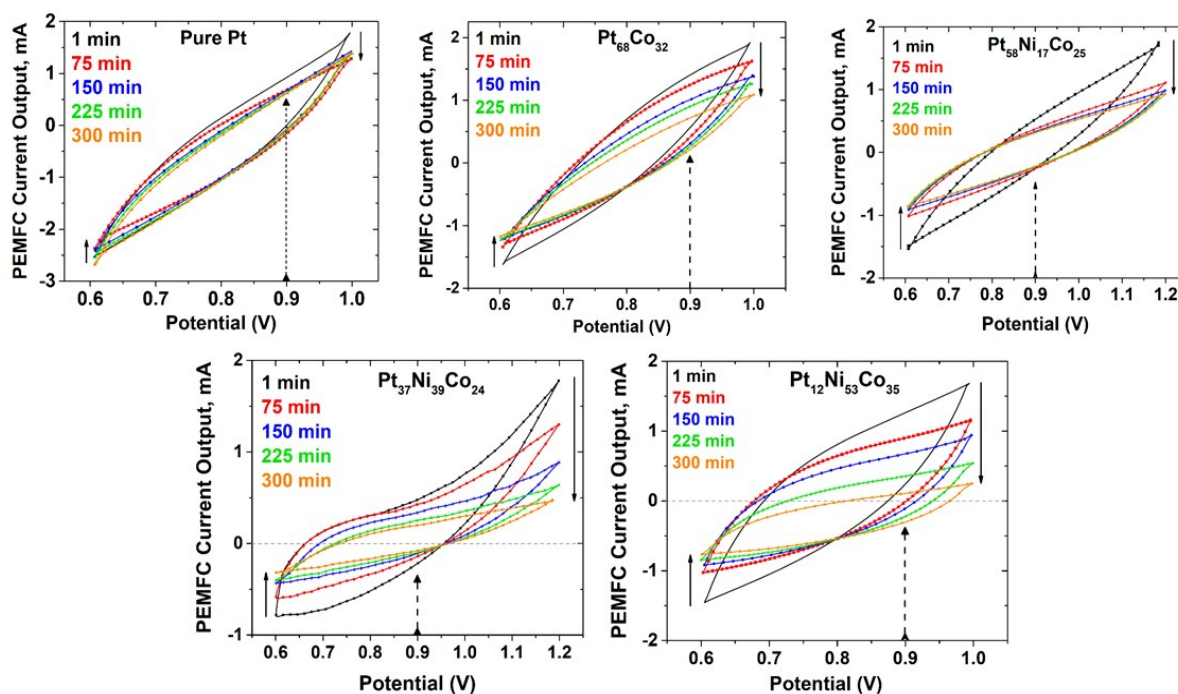


Figure S3. Selected polarization curves representing the PEMFC current output recorded during the electrochemical cycling of Pt-TM nanoalloys (TM=Co, Ni) under humidified N_2 atmosphere. The curves tend to collapse, i.e. the PEMFC current output diminishes, during the cycling (see the solid black arrows on both sides of the curves). As discussed in the text, the observation indicates a diminishing of the apparent ORR activity of studied nanoalloys during the PEMFC operation. Note that, due to a limited display of the diffusion limited current as well as potential difference due to IR drops, the CV curves look like a loop, i.e. near featureless in the particular narrow window of fast potential cycling (0.6 to 1.0 V). The CV curves definitely do not exhibit a pure resistor's behavior but are related to Pt oxidation/reduction reactions. That is because a pure resistor would show much smaller currents with a much smaller rectangular-like loop. Indeed, the polarization curves presented here resemble very much curves reflecting the kinetics of formation and reduction of surface oxide for Pt catalysts cycled inside PEMFCs under humidified N_2 atmosphere (e.g. see Figure 3 in ref.[S5]). As an example, changes (in %) in the area of the curves for cycled $Pt_{12}Ni_{53}Co_{35}$ NPs, which are related to changes in the oxidation/reduction charge during the PEMFC operation [S14], are shown in Figure S4. As can be seen in the Figure, relative changes in the PEMFC current output at 0.9 V on the polarization curves and area of the respective curves with the potential cycling are highly correlated, providing a consistent picture of the evolution of the apparent ORR activity of studied Pt-TM nanoalloys under operating conditions.

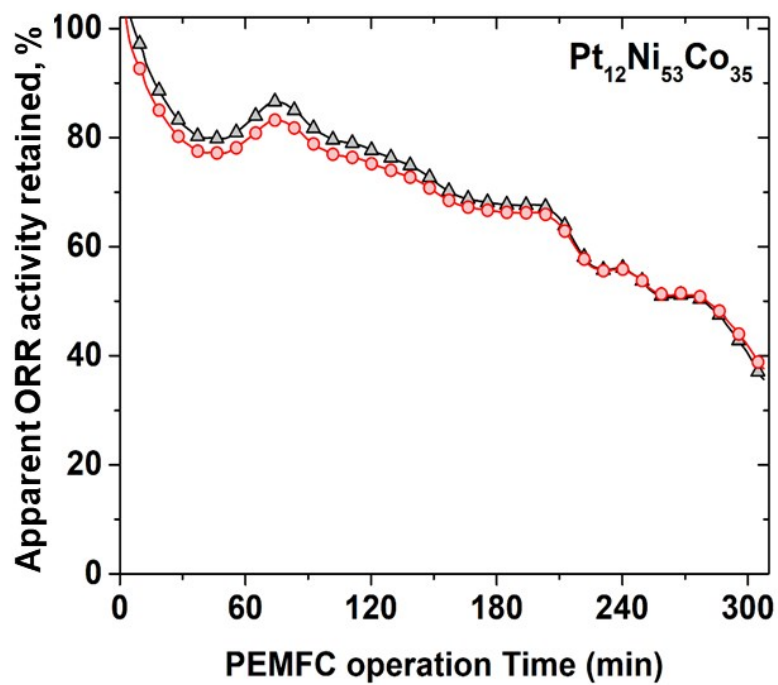


Figure S4. Relative changes in the apparent ORR activity of cycled Pt₁₂Ni₅₃Co₃₅ NPs. The changes are evaluated from the decay of the PEMFC “redox” current at 0.9 V on polarization curves (dark triangles) and collapse of the area of the respective polarization curves (red circles). The latter is related to changes in the oxidation/reduction charge during the PEMFC cycling [S14].

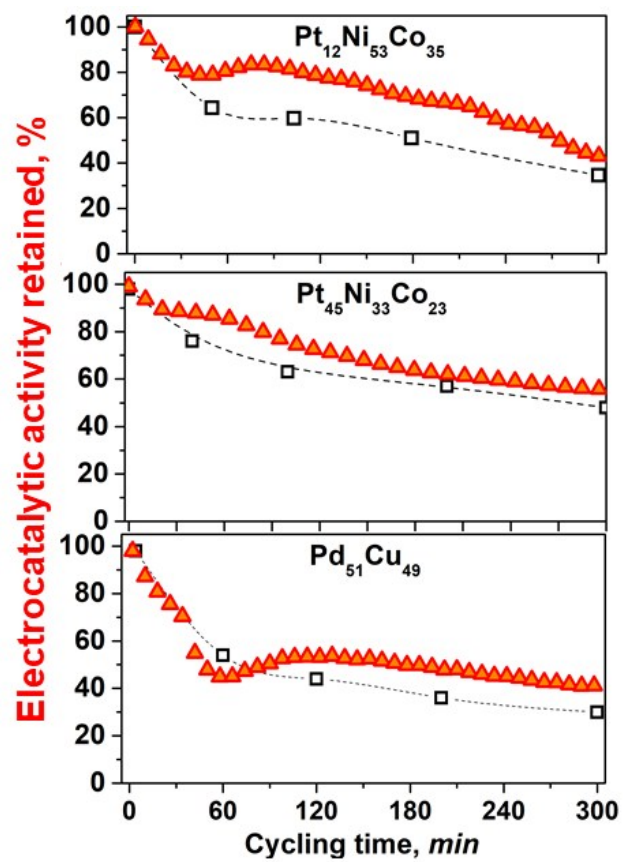
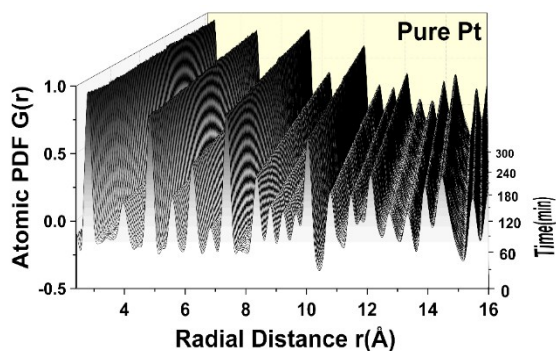


Figure S5. Relative change in the electrocatalytic activity of Pt-TM nanoalloys cycled inside a PEMFC (red triangles), as derived from the decay of the PEMFC “redox” current output at 0.9 V on the respective polarization curves. Relative change in the electrocatalytic activity of the same nanoalloys (black squares), as derived from data obtained on a standard 3-electrode laboratory cell. Laboratory cycling has been done between 0.6-1.2 V (vs. RHE) in N₂-saturated 0.1 M HClO₄ solution. The respective ORR activity values are determined by measuring the kinetic current of RDE curves at 0.8 V vs. RHE in O₂ saturated 0.1 M HClO₄ solution. Dotted black line is a guide to the eye. Trends of data for relative changes in electrocatalytic activity obtained by *in operando* and Lab experiments are seen to agree rather well. Note that *in operando* data for Pt₁₂Ni₅₃Co₃₅ NPs are those shown in Figure 6e. Data for Pt₄₅Ni₃₃Co₂₃ and Pd₅₁Cu₄₉ NPs are obtained in our prior *in operando* studies described in refs. [S26 and S27].



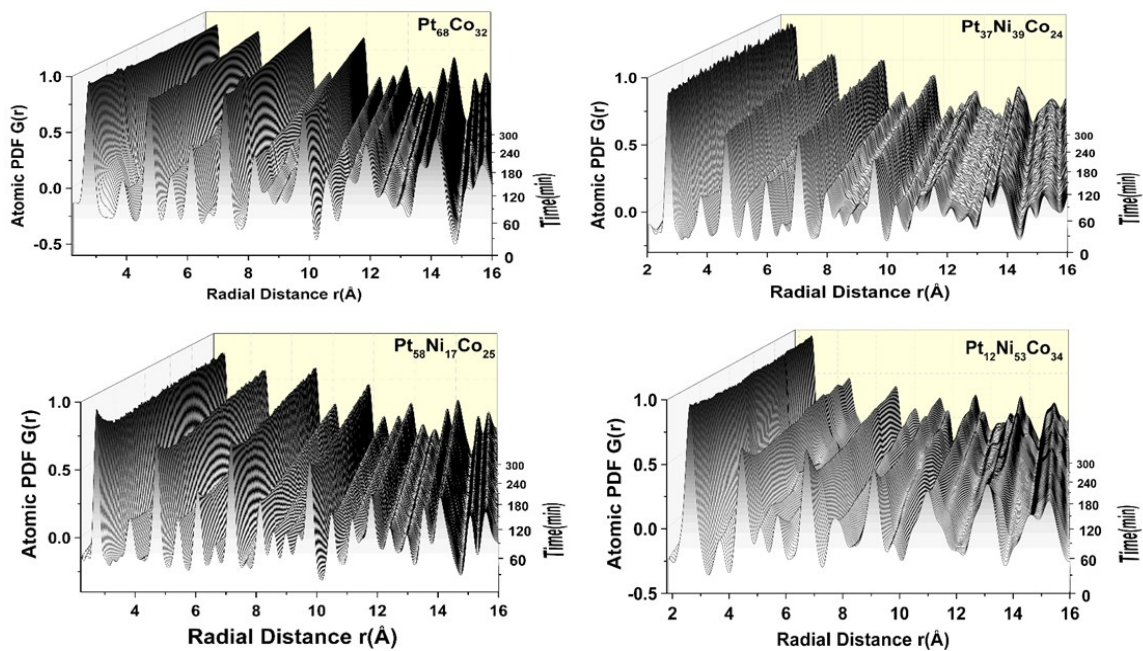


Figure S6. *In operando* atomic PDFs for pure Pt and Pt-TM alloy NPs (TM=Ni, Co) derived from the respective HE-XRD data sets shown in Figure 1.

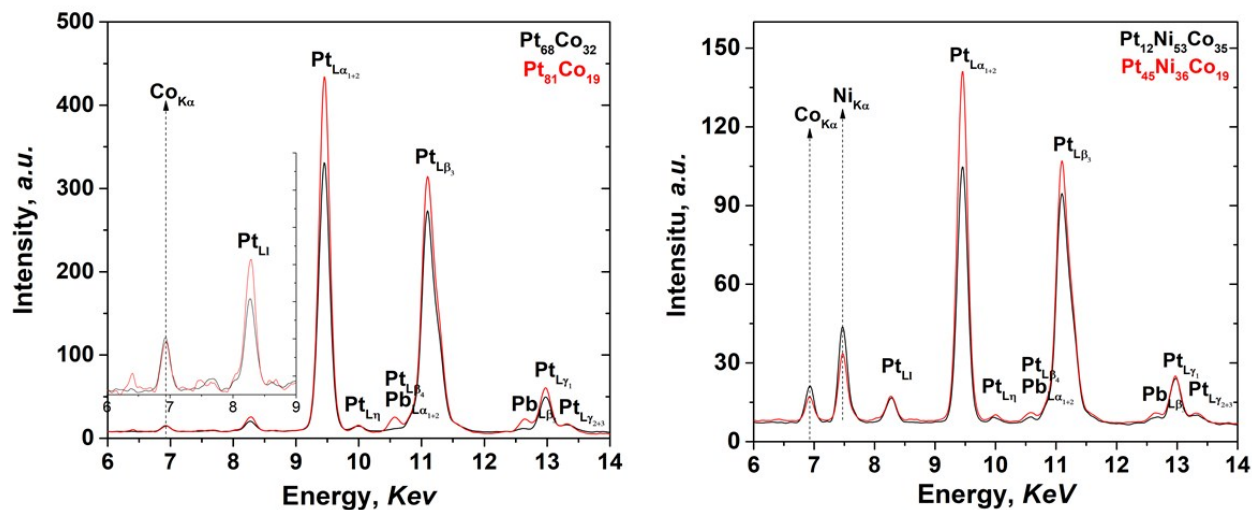


Figure S7. Exemplary EDS spectra for (black line) fresh and (red line) 300 min cycled (~1600 cycles) Pt-TM alloy NPs (TM=Ni, Co). Relative changes in the intensity of spectral lines (follow the vertical arrows) reflect changes in the chemical composition of the NPs. The changes are due to leaching of TM species induced by the highly corrosive conditions at the PEMFC cathode. Note that values for the chemical composition of fresh NPs determined by the independent ICP-AES and EDX experiments carried out here are virtually the same.

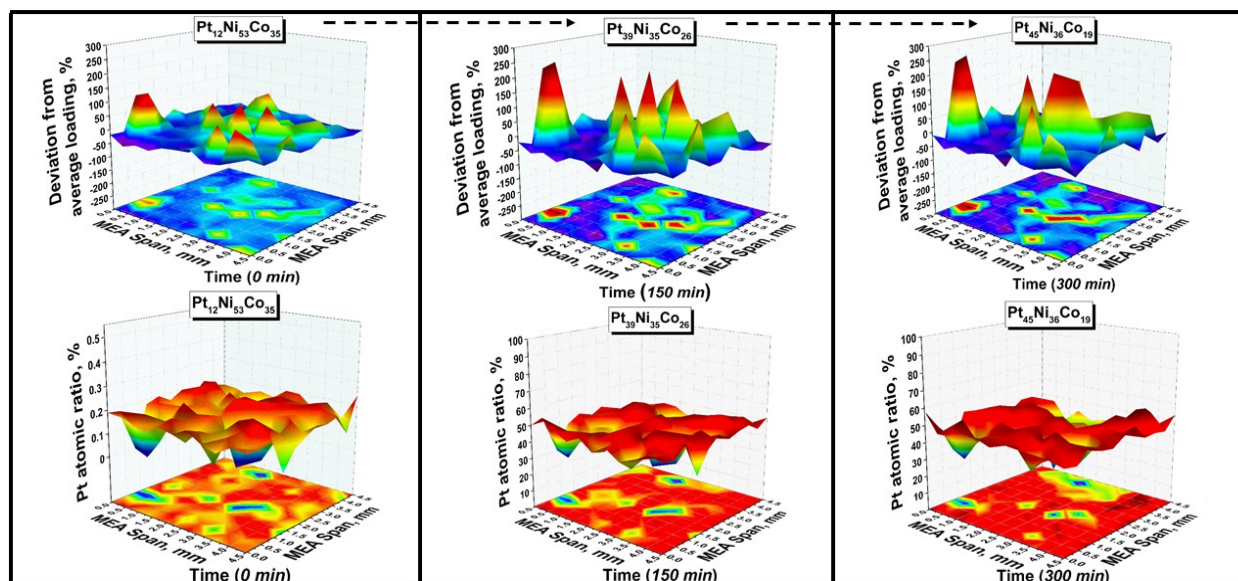


Figure S8. (first row) Mass distribution (loading) of fresh (left), 150 min (middle) and 300 min (right) cycled Pt₁₂Ni₅₃Co₃₅ alloy NPs over a 4.5 mm x 4.5 mm area of the MEA. The distribution is irregular showing large fluctuations (up to ~ 200 %) from the average catalyst loading for that area. (second row) Distribution of Pt species over the same MEA area. The distribution is normalized against the average chemical composition of the NPs, as determined by EDS. Note that, due to leaching of both Ni and Co species during the PEMFC operation, the average chemical compositions of the NPs changes from Pt₁₂Ni₅₃Co₃₅ to (300 min cycled) Pt₄₅Ni₃₆Co₁₉ (follow the dotted arrows). Nevertheless, the chemical composition of the NPs at different spots of the membrane do not exhibit large fluctuations about the average value.

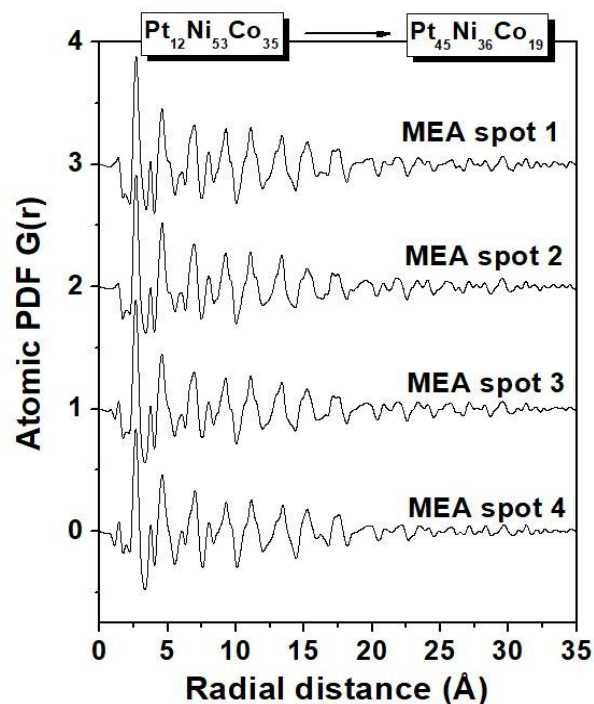


Figure S9. *In operando* atomic PDFs for $\text{Pt}_{12}\text{Ni}_{53}\text{Co}_{35}$ alloy NPs undergone 5 hours of potential cycling inside the operating PEMFC. As a result, the average chemical composition of the NPs has changed to $\text{Pt}_{45}\text{Ni}_{36}\text{Co}_{19}$, as determined by EDS (see Figure S7). The PDFs are derived from HE-XRD data sets collected from 4 different spots of the MEA, whereat the mass loading the NPs exhibits large fluctuations about the average value. The PDFs are near identical indicating that the NPs at the respective spots have a very similar atomic-scale structure.

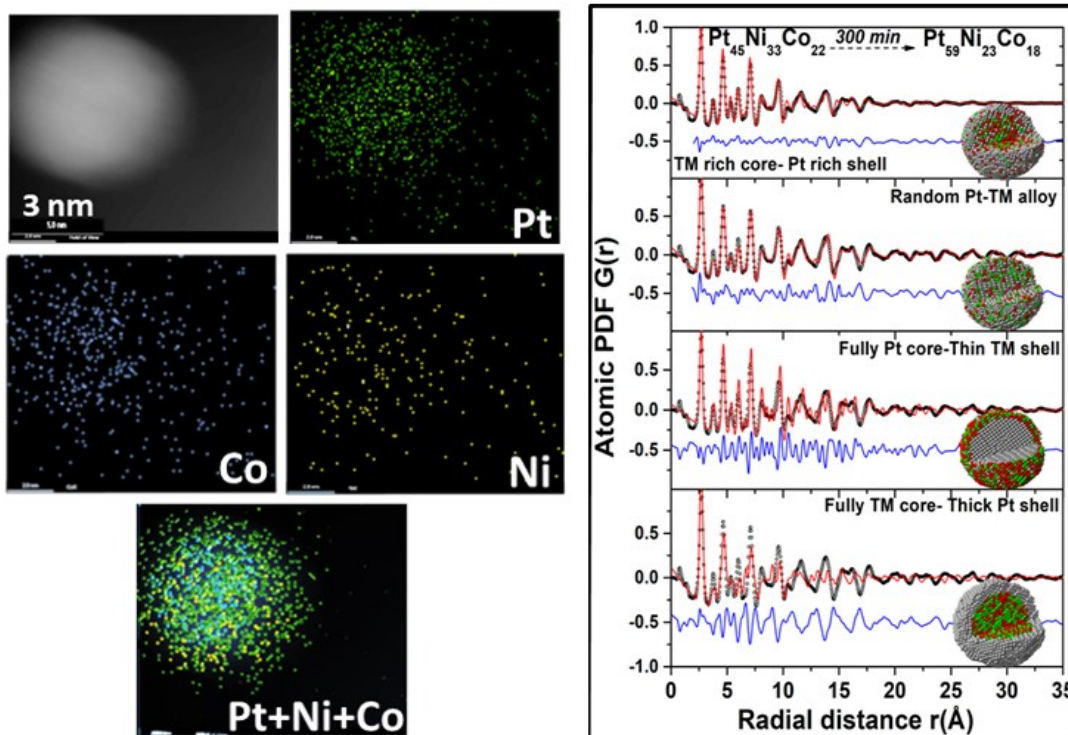


Figure S10. (*left*) Representative HAADF-STEM image and elemental maps of Pt₄₅Ni₃₃Co₂₂ nanoparticle cycled for 300 min. The maps indicate that the cycled particles are likely to possess a TM rich core-Pt rich shell type structure. (*right*) *In operando* (symbols) and computed (red line) atomic PDFs for the NPs. The computed PDFs are derived from structure models shown as insets. Residual difference (blue line) between the experimental and model computed PDFs is shifted by a constant factor for clarity. Among others, a model featuring a particle with a core and shell somewhat rich TM and Pt species, respectively, approximates the experimental data to an acceptable level. The agreement between the findings of independent HAADF-STEM and structure modeling studies testifies to the reliability of “nanophase” analysis based on atomic PDFs. Pt, Co and Ni atoms are in gray, green and red, respectively. Note that due to leaching of TM species during the potential cycling, the chemical composition of Pt₄₅Ni₃₃Co₂₂ NPs changes to Pt₅₉Ni₂₃Co₁₈ (follow the horizontal broken line).

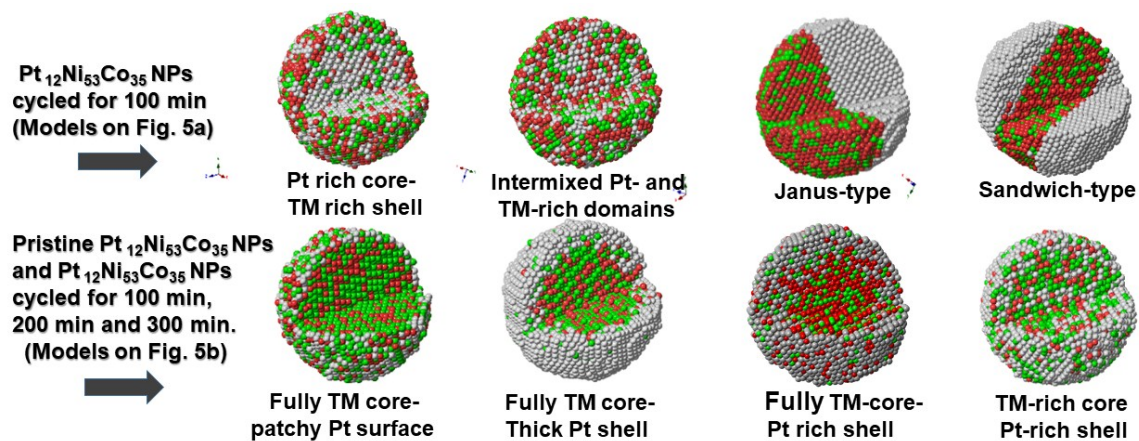


Figure S11. Larger size rendition of the structure models shown in Figure 5. The models feature ~ 8.7 nm fcc particles with a spherical shape and relevant chemical composition. Pt, Co and Ni atoms are in gray, green and red, respectively.

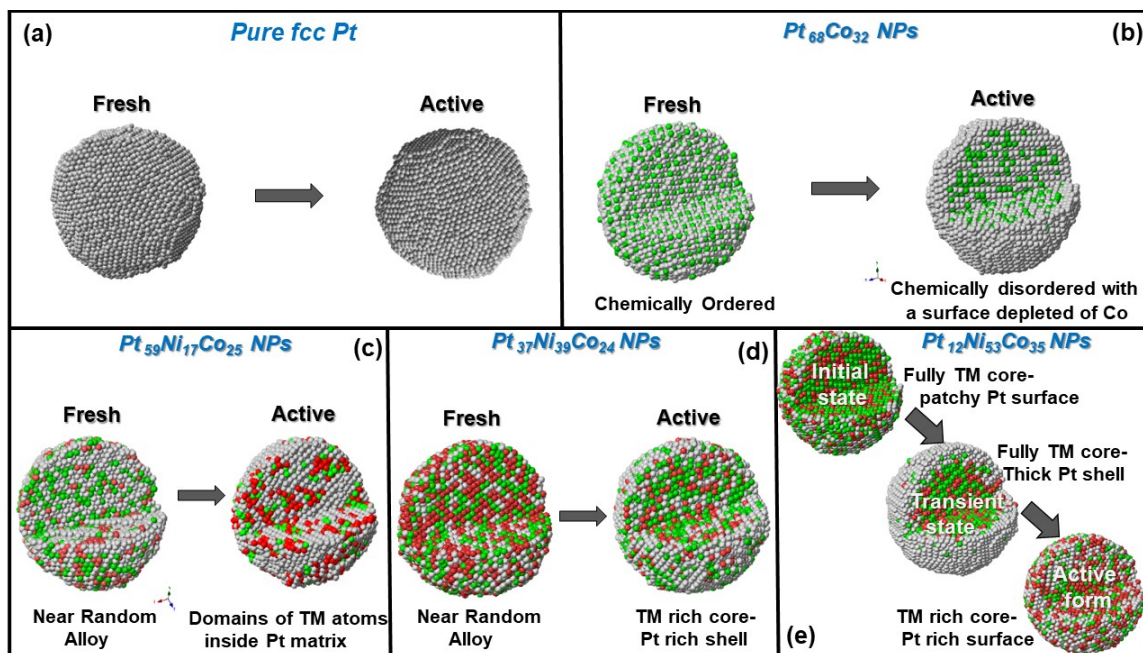


Figure S12. Larger size rendition of the 3D structure models shown in Figure 6. Models for activated and respective fresh nanoalloy catalysts are shown. The models feature ~ 8.7 nm fcc particles with a spherical shape and relevant chemical composition. Pt, Co and Ni atoms are in gray, green and red, respectively.

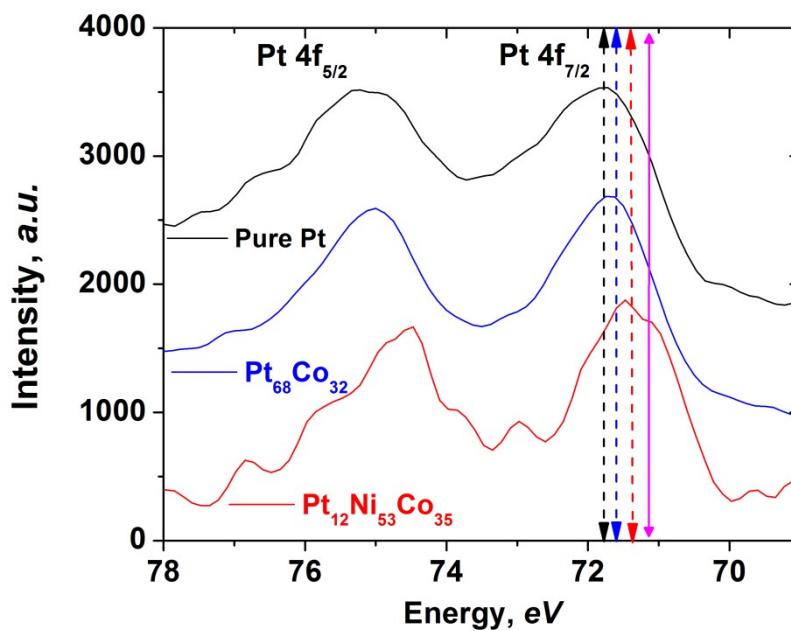


Figure S13. Typical XPS Pt 4f_{7/2} spectrum for fresh pure Pt and Pt-TM alloy NPs. Spectral lines (dotted arrows) for the NPs appear shifted to higher energies as compared to that (71.09 eV) for bulk Pt (magenta arrow). Furthermore, the shifts for the different NPs appear different in magnitude. Note that the Pt 4f_{5/2} spectral line is also seen at a higher binding energy.

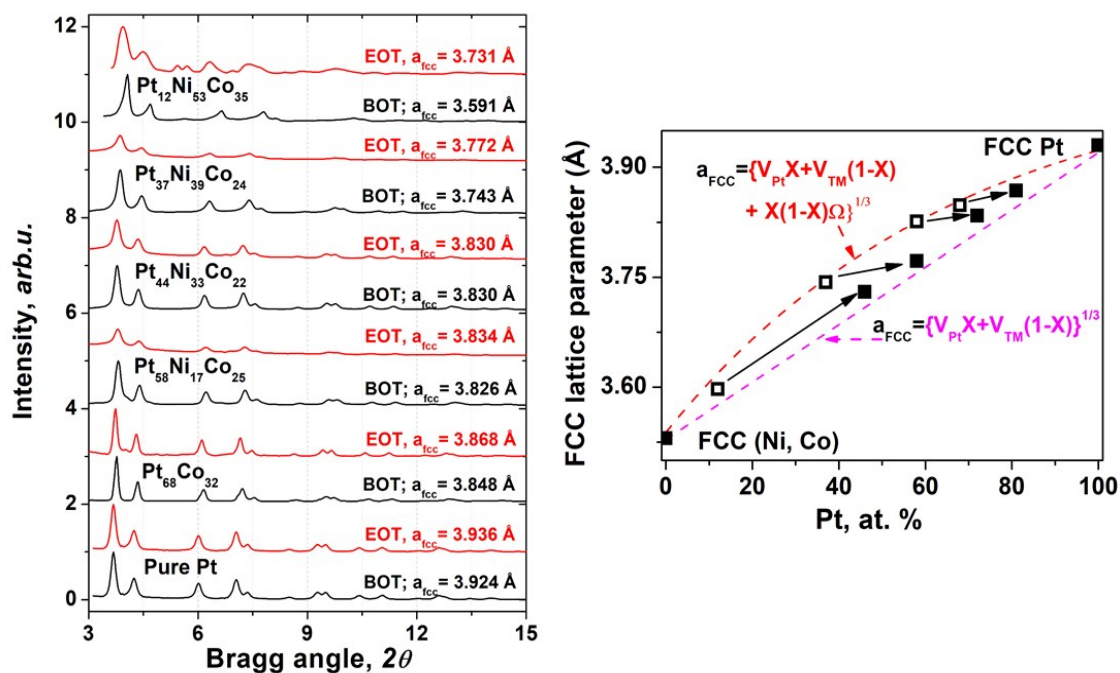


Figure S14. (left) *In situ* HE-XRD patterns for 300 min cycled (End-of-Test /EOT/red line) and respective fresh (Beginning-of-Test/BOT/black line) Pt-TM nanoalloy catalysts (TM=Ni, Co). FCC-lattice parameters obtained from the patterns using Rietveld refinement are shown for each data set. (right) FCC-lattice parameters for 300 min cycled (closed symbols) and respective fresh (open symbols) catalysts vs. their chemical composition expressed in terms of Pt percentage. The percentage is obtained by ICP-AES and confirmed by EDS. The parameters are obtained from the HE-XRD patterns on the left. Solid black arrows link data for a given pair of fresh and cycled catalyst. Magenta dotted line represents the expected composition dependence of the lattice parameter for Pt-TM alloy obtained from the elemental volumes of the intermixed atomic species (eq. 3 in the text). Red dotted line represents the expected composition dependence of the lattice parameter for Pt-TM alloy obtained from the elemental volumes of the intermixed atomic species plus a quadratic correction term involving a quantity Ω referred to as an “excess volume” in the text (eq. 4 in the text).

Table S1. Fcc-lattice parameter and nanoalloy type of fresh and 300 min cycled Pt-TM NPs obtained by a traditional analysis of their atomic PDFs. The question mark (?) indicates an increased level of uncertainty concerning the nanoalloy type. The uncertainty arises from the decreased quality of the respective fcc lattice-constrained fits.

Composition fresh/cycled	Fcc lattice parameter fresh/cycled	Structure type fresh/cycled
Pt/Pt	3.920 Å/3.924 Å	fcc/fcc
Pt ₆₈ Co ₃₂ / Pt ₈₁ Co ₁₉	3.855 Å/3.862 Å	fcc ordered alloy/ fcc disordered alloy
Pt ₅₈ Ni ₁₇ Co ₂₅ / Pt ₇₂ Ni ₁₆ Co ₁₂	3.825 Å/3.838 Å	fcc disordered (?) alloy/ fcc disordered (?) alloy
Pt ₃₇ Ni ₃₉ Co ₂₄ / Pt ₅₆ Ni ₁₆ Co ₂₆	3.750 Å/3.789 Å	fcc disordered (?) alloy fcc disordered (?) alloy
Pt ₁₂ Ni ₅₃ Co ₃₅ / Pt ₄₀ Ni ₃₉ Co ₂₁	3.639 Å/3.740 Å	fcc disordered (?) alloy fcc disordered (?) alloy